

See discussions, stats, and author profiles for this publication at: <https://www.researchgate.net/publication/259781305>

Reaction mechanism of CO activation and methane formation on Co Fischer–Tropsch catalyst: A combined DFT, transient, and steady-state kinetic modeling

ARTICLE in JOURNAL OF CATALYSIS · DECEMBER 2013

Impact Factor: 6.92 · DOI: 10.1016/j.jcat.2013.05.018

CITATIONS

17

READS

87

6 AUTHORS, INCLUDING:



Jia Yang

Norwegian University of Science and Technol...

22 PUBLICATIONS 252 CITATIONS

SEE PROFILE



Yanying Qi

Norwegian University of Science and Technol...

5 PUBLICATIONS 30 CITATIONS

SEE PROFILE



Yi-An Zhu

East China University of Science and Technology

32 PUBLICATIONS 341 CITATIONS

SEE PROFILE



De Chen

Norwegian University of Science and Technol...

235 PUBLICATIONS 4,775 CITATIONS

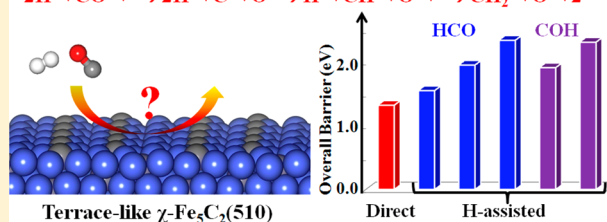
SEE PROFILE

CO Activation Pathways of Fischer–Tropsch Synthesis on χ -Fe₅C₂ (510): Direct versus Hydrogen-Assisted CO DissociationThanh Hai Pham,[†] Xuezhi Duan,^{*,†} Gang Qian,[†] Xingui Zhou,[†] and De Chen[‡][†]State Key Laboratory of Chemical Engineering, East China University of Science and Technology, 130 Meilong Road, Shanghai 200237, China[‡]Department of Chemical Engineering, Norwegian University of Science and Technology, Trondheim 7491, Norway

S Supporting Information

ABSTRACT: Iron carbides, especially χ -Fe₅C₂, among the active iron species in Fischer–Tropsch synthesis (FTS), are considered to be responsible for high FTS activity. CO activation pathways as the initial steps of FTS over χ -Fe₅C₂ were explored by spin-polarized density functional theory calculations. Surface energies of χ -Fe₅C₂ facets observed from the XRD patterns were first calculated, and then the corresponding equilibrium χ -Fe₅C₂ shape was obtained by Wulff construction. The thermodynamically stable (510) surface was predicted to have the largest percentage among the exposed crystal facets. Subsequently, the adsorption properties of CO on χ -Fe₅C₂ (510) were studied. Despite exhibiting lower binding energy than that at the 3F-4 site as the most stable configuration, CO adsorption at the 4F-1 site led to significant weakening of the C–O bond from both the structural and electronic properties' points of view. Furthermore, two kinds of CO activation mechanisms (i.e., the direct and H-assisted CO dissociation) and the corresponding six kinds of CO activation pathways on χ -Fe₅C₂ (510) were comparatively investigated on the basis of the evolution of carbon species, in which the C–O bond cleavage and further hydrogenation of surface species were concerned. The systematic analysis of the activation properties of CO suggests the direct CO dissociation as the preferred activation pathway.

Preferred pathway:



1. INTRODUCTION

Fischer–Tropsch synthesis (FTS), using coal-, natural gas-, and biomass-derived syngas as a feedstock, provides an alternative route for the production of clean fuels and key building blocks of chemical industry (e.g., lower olefins).^{1–6} This process principally uses Ru-, Co-, and Fe-based catalysts.⁷ In terms of cost, Co- and Fe-based catalysts are more attractive owing to the low price and high availability. Compared to Co-based catalysts, Fe-based FTS catalysts are especially suitable not only for the conversion of syngas (usually containing more contaminants and being CO-rich) derived from coal or biomass, owing to the higher resistance to contaminants, selectivity to olefins, and activity of water-gas shift, but also for the high temperature FTS above 300 °C with a low methanation activity.^{8,9} However, Fe-based catalysts inevitably undergo the carburization process to form a series of iron carbides (e.g., ϵ -Fe₂C, ϵ' -Fe_{2.2}C, χ -Fe₅C₂, θ -Fe₃C, and Fe₇C₃) during the pretreatment steps and FTS processes.^{10,11} Among the active iron species, Hägg iron carbide (χ -Fe₅C₂) is suggested to be responsible for the high activity of FTS.^{12–14}

CO activation is a key step in the initiation of the FTS,^{15–21} and thus a fundamental understanding of CO activation pathways is of paramount importance. In principle, the dissociation of the C–O bond may occur through either of two activation mechanisms: (i) the direct CO dissociation mechanism and (ii) the H-assisted CO dissociation mechanism.

Recently, some theoretical evidence demonstrated that CO activation mainly proceeds by the H-assisted CO dissociation via HCO intermediate on the χ -Fe₅C₂ (010)_{0.25} and χ -Fe₅C₂ (001) surfaces,^{22,23} while by H-assisted CO dissociation via COH intermediate on the χ -Fe₅C₂ (100)_{0.05} surface.²⁴ In these studies, the low Miller index and stepped-like surfaces were concerned. However, to our knowledge, the preferred pathway for CO dissociation on high Miller index surfaces has not been reported previously.

Unlike the high Miller index surfaces of monocomponent FTS catalysts (e.g., Ru, Fe, and Co) which usually have high surface energies and are difficult to be exposed, some high Miller index surfaces of bicomponent χ -Fe₅C₂ have lower surface energies.²⁵ In principle, these high Miller index surfaces are expected to be mostly exposed in the equilibrium shape of χ -Fe₅C₂ crystallite. Previous experimental results showed that some high Miller index surfaces, especially χ -Fe₅C₂ (510), were detected by XRD and HRTEM.^{14,26,27}

In this work, we employed spin-polarized density functional theory (DFT) calculations to investigate the direct and H-assisted CO dissociation on χ -Fe₅C₂ (510), aiming for discriminating the activation mechanism of CO on this high

Received: March 4, 2014

Revised: April 17, 2014

Published: April 23, 2014

Table 1. Comparison of the Calculated Lattice Parameters and the Average Magnetic Moment per Iron Atom Obtained in This Work for the Monoclinic χ -Fe₅C₂ Phase with Previous Experimental and Theoretical Values

method	<i>a</i> (Å)	<i>b</i> (Å)	<i>c</i> (Å)	β (deg)	magnetic moment (μ_B)	ref
experiment	11.588	4.579	5.059	97.75	1.72–1.75 ³⁹	26
PAW-PBE	11.580	4.508	4.994	96.64	1.73	40
PAW-PBE	11.545	4.496	4.982	97.60	1.73	25
PAW-PBE	11.554	4.502	4.985	97.62	1.73	this work

Miller index surface. The surface energies of 11 facets observed from the XRD patterns^{14,26,27} were first calculated, and the corresponding equilibrium shape of χ -Fe₅C₂ crystallite was obtained by Wulff construction, in which the thermodynamically stable (510) surface has the largest percentage among the exposed crystal facets. Then, possible adsorption configurations of CO on χ -Fe₅C₂ (510) were identified, and a systematic analysis of the CO adsorption properties, i.e., the structural and electronic properties, was further performed. Subsequently, the direct and H-assisted CO dissociation involving HCO or COH intermediate on χ -Fe₅C₂ (510), including the C–O bond cleavage and further hydrogenation of surface species, were comparatively investigated on the basis of the evolution of carbon species, suggesting the direct CO dissociation (i.e., the carbide mechanism) as the preferred activation pathway.

2. COMPUTATIONAL DETAILS

2.1. Methods. All calculations were performed by using the periodic spin-polarized DFT within the Vienna Ab initio Simulation Package (VASP).^{28–31} The electron–ion interactions were described by the projector augmented wave (PAW) method,³² and the exchange correlation energy of the electrons was treated with the GGA-PBE functional.^{33,34} The solution of the Kohn–Sham equations was expanded in a plane wave basis set with a cutoff energy of 400 eV, and the sampling of the Brillouin zone was performed using a Monkhorst–Pack scheme.³⁵ Electron smearing was employed via the Methfessel–Paxton technique with a smearing width consistent to 0.2 eV.³⁶

The dimer method³⁷ was used to determine the transition states of the elementary steps of CO activation pathways. In all the calculations, a force-based conjugated-gradient method was used to optimize the geometries.³⁸ The saddle points and minima were considered to be converged when the maximum force in every degree of freedom was less than 0.03 eV/Å. Furthermore, the vibrational frequencies were analyzed to evaluate if a stationary point is a minimum state with no imaginary frequencies or a transition state with only one imaginary frequency.

The surface energy was determined by $E_{\text{surf}} = (E_{\text{slab}} - NE_{\text{bulk}})/2A$, where E_{slab} and E_{bulk} are the total energies of the slab and one bulk unit cell, respectively, N is the number of bulk units in the slab, and A is the surface area of the slab. The adsorption energy was defined as $E_{\text{ads}} = E_{(\text{adsorbates+slab})} - (E_{\text{slab}} + E_{\text{adsorbates}})$, where $E_{(\text{adsorbates+slab})}$ is the total energy of the slab with adsorbates, E_{slab} is the total energy of the corresponding bare slab, and $E_{\text{adsorbates}}$ is the total energy of free adsorbates. In principle, the more negative is the E_{ads} , the stronger is the adsorption. The reaction energy and barrier are calculated by $\Delta E_r = E_{\text{FS}} - E_{\text{IS}}$ and $E_a = E_{\text{TS}} - E_{\text{IS}}$, respectively, where E_{IS} , E_{TS} , and E_{FS} are the energies of the corresponding initial state (IS), transition state (TS), and final state (FS), respectively. Moreover, the zero point energy (ZPE) was taken into account for all the calculated energy data.

2.2. Models. Bulk χ -Fe₅C₂ is a monoclinic crystal, and its structure has C2/c crystallographic symmetry and contains 20 Fe and 8 C atoms per unit cell. There are three types of iron atoms in the unit cell with the Wyckoff positions Fe1 (*x*1, *y*1, *z*1) (8f), Fe2 (*x*2, *y*2, *z*2) (8f), Fe3 (0, *y*3, 0.25) (4e), and one type of carbon atom C (*x*4, *y*4, *z*4) (8f). The bulk structure of χ -Fe₅C₂ was optimized with a $2 \times 5 \times 5$ Monkhorst–Pack *k*-point mesh. The three different Fe atoms have the magnetic moments of 2.11, 1.68, and 1.08 μ_B , while the C atom has an opposite magnetic moment of $-0.10 \mu_B$. The calculated average magnetic moment on all Fe atoms inside the unit cell is 1.73 μ_B . The average magnetic moment per iron atom and the calculated lattice parameters obtained in this work for the monoclinic χ -Fe₅C₂ phase were compared with previous experimental and theoretical values. As shown in Table 1, the optimized lattice parameters and the average magnetic moment are in good agreement with previous experimental and theoretical values.

For calculating the surface energies, the influence of the slab thickness was first tested to obtain the reasonable slab thicknesses of surface models, in which the slab models with a number of formula units (Fe₅C₂) ranging from 4 to 16 per supercell and with the slab thicknesses of 7–10 Å were chosen, all atoms were allowed to relax fully in the calculations, and the vacuum gap spacing of 10 Å was used. Taking χ -Fe₅C₂ (001) and χ -Fe₅C₂ (510) surfaces for example, when the slab thickness of χ -Fe₅C₂ (001) surface increases from 9.883 to 19.765 Å and that of χ -Fe₅C₂ (510) surface from 8.165 to 16.331 Å, the differences in the surface energies for both cases are very small (Table S1).

For calculating the CO adsorption energies and activation energies, influences of the supercell size of χ -Fe₅C₂ (510) surface, the size of the Monkhorst–Pack *k*-point mesh, and the number of the relaxed atom layers were first tested to guarantee the accuracy of convergence. Typically, according to the results in Tables S2–S4, the $p(1 \times 1)$ supercell slab with four layered iron and eight layered carbon, the $4 \times 2 \times 1$ Monkhorst–Pack *k*-point mesh, and the relaxed top two-layered iron and four-layered carbon were chosen. Moreover, the vacuum gap spacing of 10 Å was used.

3. RESULTS AND DISCUSSION

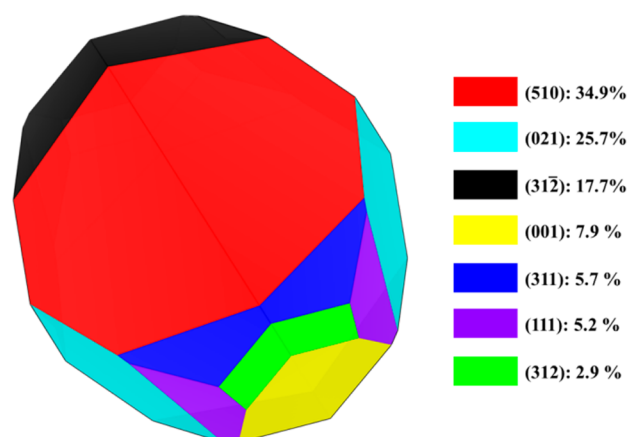
3.1. Surface Stability of χ -Fe₅C₂. Table 2 shows the surface energies of 11 facets observed from the XRD patterns.^{14,26,27} It can be seen that our computed surface energies for the low Miller index (001), (010), (101), and (111) facets of χ -Fe₅C₂ are well consistent with the previous results,^{25,40} indicating that our computational methods are reasonable. Furthermore, among the 11 facets, the high Miller index (510) facet has the lowest surface energy and thus is the thermodynamically most stable facet. It is expected that this facet could be predominant for the exposed surfaces of χ -Fe₅C₂ crystallite.

Table 2. Calculated Surface Energies of Different χ -Fe₅C₂ Facets

$2\theta^a$ (deg)	surface	surface energy (J/m ²)		
		this work	ref 25	ref 40
35.8	(001)	2.53	2.55	2.53
37.0	(311)	2.42		
39.4	(010)	2.65	2.69	2.66
40.9	(11 $\bar{2}$)	2.72		
41.2	(101)	2.85	2.88	2.86
43.5	(021)	2.14		
44.2	(510)	2.03		
45.1	(31 $\bar{2}$)	2.41		
47.3	(221)	2.62		
50.2	(312)	2.62		
58.3	(111)	2.43	2.46	2.40

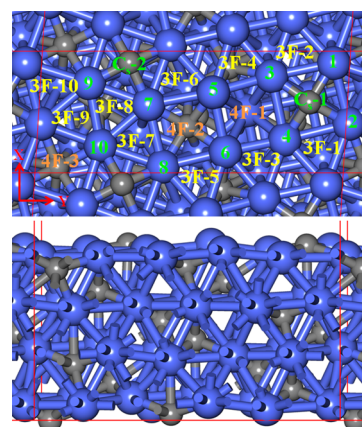
^aJCPDS No. 36-1248.

To test this idea, the Wulff construction, assuming a complete knowledge of the orientation dependence of the surface energy,⁴¹ was employed to predict the equilibrium shape of χ -Fe₅C₂ crystallite on the basis of the above surface energies. As shown in Figure 1, the obtained shape is

**Figure 1.** Equilibrium shape of χ -Fe₅C₂ obtained by Wulff construction.

polyhedral, which can be linked to the strong anisotropy in the surface energies of different χ -Fe₅C₂ facets. In addition, the thermodynamically most stable (510) facet, as expected, has the largest contribution to the total surface area of χ -Fe₅C₂ with a percentage of 34.9%.

3.2. CO Adsorption on χ -Fe₅C₂ (510) Surface. CO was systematically adsorbed at different sites of the terraced-like χ -Fe₅C₂ (510) surface with ten kinds of Fe atoms and two kinds of C atoms (Figure 2), which consist of 10 one-fold (1F), 26 2-fold (2F), 10 3-fold (3F), and 3 4-fold (4F) sites. Only nine stable adsorption configurations were obtained shown in Figure S1, in which the adsorbed CO bounded via the C atom and with the O atom pointing outward. The corresponding structural parameters and adsorption energies are summarized in Table 3. It is observed that the adsorption energies including ZPE are ranging from −1.57 to −2.03 eV. Specifically, the energies of CO adsorption at 1F sites have a large difference, while those of CO adsorption at the other sites have a slight difference. This may be because for 1F sites, Fe1 and Fe7 are closer to the surface C than Fe5 and Fe6, and thus CO

**Figure 2.** Top and side views of χ -Fe₅C₂ (510) surface. Blue and gray spheres correspond to Fe and C atoms, respectively.

molecules adsorbed on Fe1 and Fe7 have stronger repulsive interaction with the surface C. Moreover, the vibrational frequencies of CO were observed to systematically decrease when going from 1F to 4F configurations. Such variations were found to be associated with the increase in the C–O bond length with the number of surface Fe atoms. It can be concluded that despite exhibiting lower adsorption energy than that at 3F-4 site as the most stable configuration, the CO adsorption at 4F-1 site leads to significant weakening of the C–O bond, as reflected by the large C–O bond elongation and the red-shift of the vibrational frequency.

To further understand the C–O weakening behavior behind the peculiar CO adsorption on χ -Fe₅C₂ (510), LDOS (i.e., local density of state) projected onto the C–O bonds were calculated, aiming for correlating the weakening of the C–O bond with the electronic structure. Figure 3 shows the LDOS results for three typical configurations of CO adsorption at 1F-5, 3F-4, and 4F-1 sites as well as free CO. It can be clearly seen that the bands of the adsorbed CO shift downward compared to those of the free CO. The primary shifting of the 5 σ and 2 π^* bands is due to the electron forward-donation from 5 σ orbital of CO to 3d orbital of Fe and the back-donation from 3d orbital of Fe to 2 π^* orbital of CO.⁴² The integral calculations show that the electron population of 2 π^* antibonding orbital for the CO adsorbed at 1F-5, 3F-4, and 4F-1 sites are 0.50, 0.80, and 0.99 electrons, respectively. In principle, the more is the electrons transferring from the Fe atom to the adsorbed CO antibonding orbital, the more significant is the weakening of the C–O bond.^{43,44} Therefore, CO adsorption at 4F-1 site shows the most significant weakening of the C–O bond.

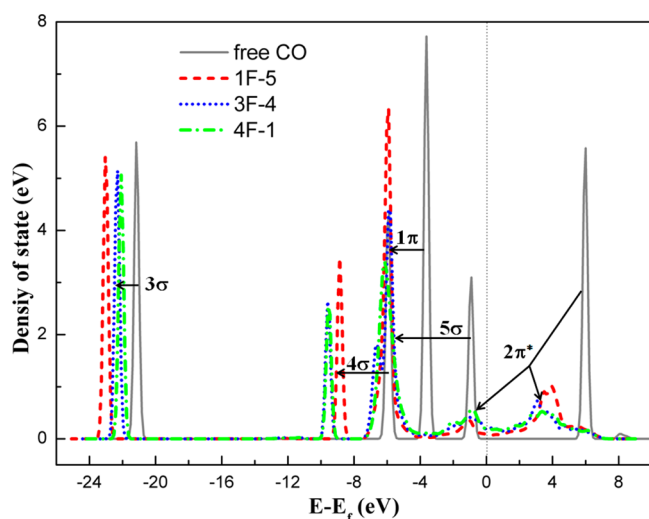
To sum up the above analyses, no matter from the structural or electronic properties' points of view, CO adsorption at 4F-1 site shows the significant weakening of the C–O bond. This suggests that the 4F-1 configuration is most likely considered as a precursor state for CO dissociation.

3.3. CO Activation Pathways on χ -Fe₅C₂ (510) Surface.

It is well-known that two kinds of mechanisms, i.e., the direct CO dissociation (i.e., the carbide mechanism) and the H-assisted CO dissociation mechanism, are proposed for CO activation in the FTS process.^{17–19,21} When taking the type of surface intermediates into account, the latter mechanism will be divided into two pathways: the H-assisted CO dissociation via HCO intermediate and H-assisted CO dissociation via COH intermediate. Furthermore, these intermediates may be further decomposed by the cleavage of the C–O bond and

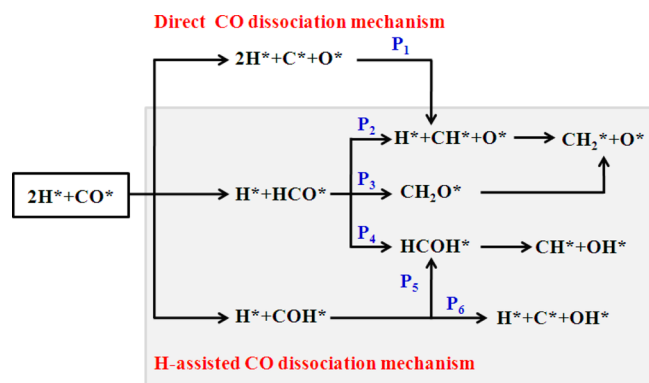
Table 3. Structural Parameters and Adsorption Energies (E_{ads} Values Including ZPE in Parentheses) for CO Adsorbed on χ -Fe₅C₂ (510) Surface

sites	$r_{(\text{Fe}-\text{C})}$ (Å)			E_{ads} (eV)	$\nu_{(\text{C}-\text{O})}$ (cm ⁻¹)	$r_{(\text{C}-\text{O})}$ (Å)
1F-1	1.768			-1.66 (-1.57)	1955	1.168
1F-5	1.780			-2.10 (-2.01)	1933	1.172
1F-6	1.765			-2.05 (-1.97)	1906	1.177
1F-7	1.763			-1.67 (-1.58)	1953	1.169
2F	2.207	1.813		-1.99 (-1.92)	1819	1.189
3F-3	2.120	2.101	1.858	-1.99 (-1.93)	1726	1.201
3F-4	2.067	2.024	1.948	-2.08 (-2.03)	1727	1.200
3F-9	2.277	2.014	1.885	-1.97 (-1.91)	1760	1.196
4F-1	2.305	2.245	2.024	-1.99 (-1.93)	1640	1.214

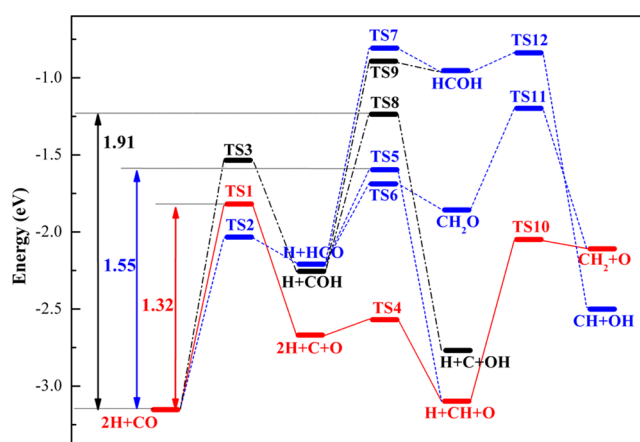
**Figure 3.** LDOS of CO adsorbed at 1F-5, 3F-4, and 4F-1 sites as well as free CO.

hydrogenated by the second hydrogenation step. Comprehensively concerning the above possibilities, six kinds of CO activation pathways in the FTS process are yielded and schematically shown in Figure 4, in which only the evolution of carbon species is presented.

Subsequently, the dissociation properties of CO involving in the six kinds of CO activation pathways on χ -Fe₅C₂ (510) were comparatively studied. The energy profiles for the direct or H-

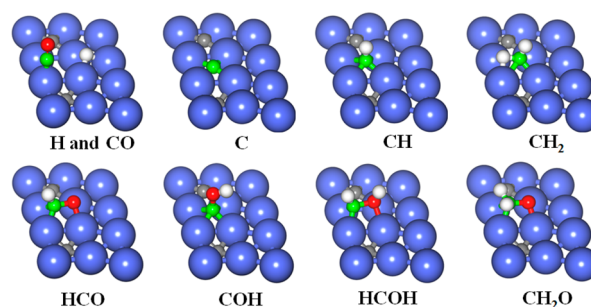
**Figure 4.** Schematic of two kinds of CO activation mechanisms and the corresponding six kinds of CO activation pathways (i.e., P₁–P₆) in the FTS process. H-assisted CO dissociation mechanism was labeled by a rectangular shadow, and the empty site (*) was not presented for the sake of clarity.

assisted dissociation of CO from coadsorbed H and CO on χ -Fe₅C₂ (510) surface are shown in Figure 5. In addition, the

**Figure 5.** Energy profiles for the direct or H-assisted dissociation of CO from coadsorbed H and CO on χ -Fe₅C₂ (510) surface. The energies are given in eV with respect to gas-phase CO + H₂. Red line (solid): direct CO dissociation; blue line (dash): H-assisted CO dissociation via HCO intermediate; black line (dash dot): H-assisted CO dissociation via COH intermediate.

most stable configurations of the coadsorbed CO and H and carbon-containing intermediates are illustrated in Figure 6, and the transition state structures are given in Figure 7.

For the P₁ pathway (i.e., the direct CO activation pathway), the CO molecule is preactivated in the adsorbed state from 1F-5 to 4F-1 sites with the more detailed description shown in section 3.2, while the H atom diffuses from 3F-3 to 3F-5 sites.

**Figure 6.** Most stable configurations of the coadsorbed CO and H and carbon-containing intermediates involved in the direct or H-assisted CO dissociation on χ -Fe₅C₂ (510) surface. Blue: Fe atoms; gray: C atoms of iron carbide; green: C atoms of adsorbates; red: O atoms; white: H atoms.

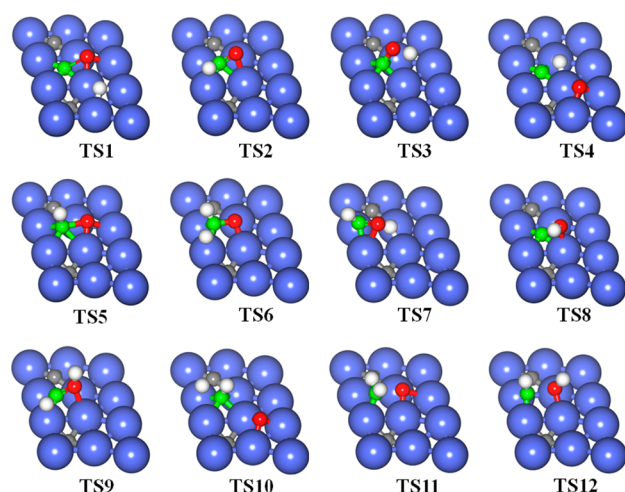


Figure 7. Structures of the transition states of elementary steps involved in the direct or H-assisted CO dissociation from coadsorbed H and CO on χ -Fe₅C₂ (510) surface. Blue: Fe atoms; gray: C atoms of iron carbide; green: C atoms of adsorbates; red: O atoms; white: H atoms.

The CO in the transition state (i.e., TS1) is situated at a stable 5-fold site, in which the C and O atoms share two Fe atoms and the C–O bond length increases up to 1.694 Å. These factors lead to a CO dissociation barrier of 1.32 eV (Figure 5). Moreover, after traversing the TS, the C, O, and H atoms in the final state (FS) are found to situate at 4F-1, 3F-3, and 3F-5 sites, respectively. The direct CO dissociation is endothermic by 0.48 eV and thus thermodynamically occurs under FTS conditions.

Regarding the H-assisted CO activation pathways via HCO intermediate (i.e., P₂, P₃, and P₄), the reaction of H and CO to form HCO is observed to be highly endothermic by 0.94 eV and has a hydrogenation barrier of 1.11 eV, lower than the barrier for the direct CO dissociation. Herein, we further study the C–O bond dissociation followed by hydrogenation or the hydrogenation followed by C–O bond dissociation of the HCO intermediate, which include three possibilities: HCO + H → CH + O + H → CH₂ + O, HCO + H → CH₂O → CH₂ + O, and HCO + H → HCOH → CH + OH (Figure 4). As shown in Figure 5, the reaction barrier of HCOH formation (i.e., 1.39 eV) is much higher than those of HCO dissociation (i.e., 0.61 eV) and CH₂O formation (i.e., 0.51 eV). Meanwhile, one should note that the overall barriers for P₂, P₃, and P₄ are 1.55, 1.95, and 2.34 eV, respectively, mainly owing the highly exothermic nature (i.e., −0.90 eV) for the HCO dissociation step in the P₂ pathway. This indicates that the P₂ pathway is more favorable than the P₃ and P₄ pathways.

Similarly, the CO properties by the direct dissociation (i.e., P₁) or the H-assisted dissociation via HCO intermediate (i.e., P₂) were further compared. To this end, the stepwise hydrogenation of the resultant C from the direct CO dissociation was calculated. Interestingly, the overall barrier for the P₁ pathway is 1.32 eV, which is 0.23 eV lower than that for the P₂ pathway. Meanwhile, in the P₂ pathway, the reverse reaction (HCO → H + CO) for the formation of HCO intermediate has a low barrier of only 0.17 eV, which is 0.44 eV lower than that for the dissociation of HCO into CH and O. These results strongly indicate that compared to the H-assisted CO dissociation via HCO intermediate, the direct CO

dissociation is predicted to be a preferential CO activation pathway.

In addition, when comparing the direct CO dissociation to the H-assisted CO dissociation via COH intermediate, we find that the H-assisted CO dissociation via COH intermediate is an energetically unfavorable pathway because the hydrogenation barrier for the formation COH (1.62 eV), the overall barrier for the P₅ pathway (1.91 eV), and the overall barrier for the P₆ pathway (2.31 eV) are higher than the overall barrier for the P₁ pathway (1.32 eV). Hence, we conclude that under typical F–T process conditions (250 °C), the P₁ pathway (i.e., the direct CO dissociation) is proposed to be as the dominant activation pathway for the CO dissociation on the χ -Fe₅C₂ (510) surface.

Table 4 gives a comparison of the preferred CO activation pathways between χ -Fe₅C₂ (510) and other χ -Fe₅C₂ surfaces

Table 4. Preferred CO Activation Pathways of Various χ -Fe₅C₂ Surfaces

surface	preferred CO activation pathway	ref
(510)	direct CO dissociation	this work
(010)-0.25	H-assisted CO dissociation via HCO intermediate	22
(001)	H-assisted CO dissociation via HCO intermediate	23
(100)-0.05	H-assisted CO dissociation via COH intermediate	24

taken from the literature.^{22–24} Obviously, the preferred CO activation pathway is the direct CO dissociation for the terraced-like χ -Fe₅C₂ (510) surface, while the H-assisted CO dissociation for the other stepped-like χ -Fe₅C₂ surfaces. Generally, the direct CO dissociation corresponds to the high FTS activity.²¹ Accordingly, the terraced-like χ -Fe₅C₂ (510) surface may have higher FTS activity than the stepped-like χ -Fe₅C₂ surfaces. This is different from the trend for the monocomponent catalysts (e.g., Co and Ru) that the direct CO dissociation is the preferred pathway on the highly active stepped surface.^{17,45} In addition, previous experimental results showed that the trend of the size effects for iron carbide is contrast with those for Co and Ru.^{46–48} This may be because the terraced-like surfaces of χ -Fe₅C₂ are active surfaces, and smaller iron carbide particles have larger surface area for the terraced-like surfaces, leading to the high FTS activity for the smaller iron carbide catalysts.

Moreover, Table 4 also sheds new light on tuning CO activation pathway by changing the crystal facet of χ -Fe₅C₂. Iglesia et al. provided experimental and theoretical evidence for the effect of CO activation pathway on oxygen rejection pathways.¹⁸ It can be concluded that manipulating the crystal facet of χ -Fe₅C₂ could be an effective method to tune the CO activation pathway and thus the products selectivity. A deep insight into the relation between χ -Fe₅C₂ crystal facet, CO activation pathway, and reactivity and products selectivity is highly desirable, which guide us to design highly efficient FTS catalysts. The work along this line is in progress in our group.

4. CONCLUSIONS

In summary, we have performed spin-polarized DFT calculations to predict the equilibrium shape of χ -Fe₅C₂ crystallite by Wulff construction based on the surface energies of 11 facets observed by XRD patterns. The thermodynamically most stable (510) facet is found to have the largest contribution to the total surface area of χ -Fe₅C₂ with a percentage of 34.9%. The systematic analysis of the adsorption properties of CO on χ -Fe₅C₂ (510) shows that despite exhibiting lower binding

energy than that at 3F-4 site as the most stable configuration, CO adsorption at 4F-1 site led to significant weakening of the C–O bond from both the structural and electronic properties' points of view.

Moreover, concerning the type of CO activation mechanisms and the evolution of surface carbon-containing intermediates, the six kinds of CO activation pathways on the terraced-like χ -Fe₅C₂ (510) surface were comparatively investigated. The direct CO dissociation mechanism is suggested to the preferred activation pathway. The insights revealed here are different from the results of the reported χ -Fe₅C₂ (010)_{0.25}, χ -Fe₅C₂ (110)_{0.00}, and χ -Fe₅C₂ (110)_{0.80} surfaces (i.e., the H-assisted CO dissociation mechanism as the preferred activation pathway), which might shed new light on optimizing the performance of χ -Fe₅C₂ catalysts by changing the crystal facets.

■ ASSOCIATED CONTENT

Supporting Information

More details of influences of the slab thickness, the supercell size, the size of Monkhorst–Pack k -point mesh and the number of relaxed atom layers, as well as top and side views of the adsorption configurations of CO on χ -Fe₅C₂ (510) surface. This material is available free of charge via the Internet at <http://pubs.acs.org>.

■ AUTHOR INFORMATION

Corresponding Author

*Tel +86-21-64250937; Fax +86-21-64253528; e-mail xzduan@ecust.edu.cn (X.D.).

Notes

The authors declare no competing financial interest.

■ ACKNOWLEDGMENTS

This work is financially supported by the Natural Science Foundation of China (21306046), the China Postdoctoral Science Foundation (2012M520041 and 2013T60428), and the 111 Project of Ministry of Education of China (B08021).

■ REFERENCES

- (1) Khodakov, A. Y.; Chu, W.; Fongarland, P. Advances in the Development of Novel Cobalt Fischer–Tropsch Catalysts for Synthesis of Long-chain Hydrocarbons and Clean Fuels. *Chem. Rev.* **2007**, *107*, 1692–1744.
- (2) Dry, M. E. The Fischer–Tropsch Process: 1950–2000. *Catal. Today* **2002**, *71*, 227–241.
- (3) Iglesia, E. Design, Synthesis, and Use of Cobalt-Based Fischer–Tropsch Synthesis Catalysts. *Appl. Catal., A* **1997**, *161*, 59–78.
- (4) Fischer, F.; Tropsch, H. The Preparation of Synthetic Oil Mixtures (Synthol) from Carbon Monoxide and Hydrogen. *Brennst.-Chem.* **1923**, *4*, 276–285.
- (5) Torres Galvis, H. M.; de Jong, K. P. Catalysts for Production of Lower Olefins from Synthesis Gas: A Review. *ACS Catal.* **2013**, *3*, 2130–2149.
- (6) Cheng, J.; Hu, P.; Ellis, P.; French, S.; Kelly, G.; Lok, C. M. Some Understanding of Fischer–Tropsch Synthesis from Density Functional Theory Calculations. *Top. Catal.* **2010**, *53*, 326–337.
- (7) Yang, J.; Ma, W.; Chen, D.; Holmen, A.; Davis, B. H. Fischer–Tropsch Synthesis: A Review of the Effect of CO Conversion on Methane Selectivity. *Appl. Catal., A* **2014**, *470*, 250–260.
- (8) Torres Galvis, H. M.; Koeken, A. C. J.; Bitter, J. H.; Davidian, T.; Ruitenbeek, M.; Dugulan, A. I.; de Jong, K. P. Effects of Sodium and Sulfur on Catalytic Performance of Supported Iron Catalysts for the Fischer–Tropsch Synthesis of Lower Olefins. *J. Catal.* **2013**, *303*, 22–30.
- (9) Steynberg, A.; Dry, M. E. *Fischer–Tropsch Technology, Series: Studies in Surface Science and Catalysis No.152*; Elsevier: Amsterdam, 2004.
- (10) de Smit, E.; Weckhuysen, B. M. The Renaissance of Iron-Based Fischer–Tropsch Synthesis: On the Multifaceted Catalyst Deactivation Behaviour. *Chem. Soc. Rev.* **2008**, *37*, 2758–2781.
- (11) Niemantsverdriet, J. W.; Van der Kraan, A. M.; Van Dijk, W. L.; Van der Baan, H. S. Behavior of Metallic Iron Catalysts During Fischer–Tropsch Synthesis Studied with Moessbauer Spectroscopy, X-ray Diffraction, Carbon Content Determination, and Reaction Kinetic Measurements. *J. Phys. Chem.* **1980**, *84*, 3363–3370.
- (12) Herranz, T.; Rojas, S.; Pérez-Alonso, F. J.; Ojeda, M.; Terreros, P.; Fierro, J. L. G. Genesis of Iron Carbides and Their Role in the Synthesis of Hydrocarbons from Synthesis Gas. *J. Catal.* **2006**, *243*, 199–211.
- (13) de Smit, E.; Cinquini, F.; Beale, A. M.; Safonova, O. V.; van Beek, W.; Sautet, P.; Weckhuysen, B. M. Stability and Reactivity of ϵ - χ - θ Iron Carbide Catalyst Phases in Fischer–Tropsch Synthesis: Controlling μ C. *J. Am. Chem. Soc.* **2010**, *132*, 14928–14941.
- (14) Yang, C.; Zhao, H.; Hou, Y.; Ma, D. Fe₅C₂ Nanoparticles: A Facile Bromide-Induced Synthesis and as an Active Phase for Fischer–Tropsch Synthesis. *J. Am. Chem. Soc.* **2012**, *134*, 15814–15821.
- (15) Ciobica, I. M.; Van Santen, R. A. Carbon Monoxide Dissociation on Planar and Stepped Ru (0001) Surfaces. *J. Phys. Chem. B* **2003**, *107*, 3808–3812.
- (16) Andersson, M. P.; Abild-Pedersen, F.; Remediakis, I. N.; Bligaard, T.; Jones, G.; Engbæk, J.; Lytken, O.; Horch, S.; Nielsen, J. H.; Sehested, J.; Rostrup-Nielsen, J. R.; Nørskov, J. K.; Chorkendorff, I. Structure Sensitivity of the Methanation Reaction: H₂-Induced CO Dissociation on Nickel surfaces. *J. Catal.* **2008**, *255*, 6–19.
- (17) Shetty, S.; Jansen, A. P. J.; van Santen, R. A. Direct versus Hydrogen-Assisted CO Dissociation. *J. Am. Chem. Soc.* **2009**, *131*, 12874–12875.
- (18) Ojeda, M.; Nabar, R.; Nilekar, A. U.; Ishikawa, A.; Mavrikakis, M.; Iglesia, E. CO Activation Pathways and the Mechanism of Fischer–Tropsch Synthesis. *J. Catal.* **2010**, *272*, 287–297.
- (19) Yang, J.; Qi, Y. Y.; Zhu, J.; Zhu, Y. A.; Chen, D.; Holmen, A. Reaction Mechanism of CO Activation and Methane Formation on Co Fischer–Tropsch Catalyst: A Combined DFT, Transient, and Steady-State Kinetic Modelling. *J. Catal.* **2013**, *308*, 37–49.
- (20) Loveless, B. T.; Buda, C.; Neurock, M.; Iglesia, E. CO Chemisorption and Dissociation at High Coverages during CO Hydrogenation on Ru Catalysts. *J. Am. Chem. Soc.* **2013**, *135*, 6107–6121.
- (21) Liu, J. X.; Su, H. Y.; Sun, D. P.; Zhang, B. Y.; Li, W. X. Crystallographic Dependence of CO Activation on Cobalt Catalysts: HCP versus FCC. *J. Am. Chem. Soc.* **2013**, *135*, 16284–16287.
- (22) Huo, C. F.; Li, Y. W.; Wang, J.; Jiao, H. Insight into CH₄ Formation in Iron-Catalyzed Fischer–Tropsch Synthesis. *J. Am. Chem. Soc.* **2009**, *131*, 14713–14721.
- (23) Cao, D. B.; Li, Y. W.; Wang, J.; Jiao, H. Chain Growth Mechanism of Fischer–Tropsch Synthesis on Fe₅C₂ (001). *J. Mol. Catal. A: Chem.* **2011**, *346*, 55–69.
- (24) Gracia, J. M.; Prinsloo, F. F.; Niemantsverdriet, J. W. Mars-van Krevelen-like Mechanism of CO Hydrogenation on an Iron Carbide Surface. *Catal. Lett.* **2009**, *133*, 257–261.
- (25) Zhao, S.; Liu, X. W.; Huo, C. F.; Li, Y. W.; Wang, J.; Jiao, H. Surface Morphology of Hägg Iron Carbide (χ -Fe₅C₂) from Ab initio Atomistic Thermodynamics. *J. Catal.* **2012**, *294*, 47–53.
- (26) Retief, J. J. Powder Diffraction Data and Rietveld Refinement of Hägg-Carbide χ -Fe₅C₂. *Powder Diffr.* **1999**, *14*, 130–132.
- (27) Huang, G.; Hu, J.; Zhang, H.; Zhou, Z.; Chi, X.; Gao, J. Highly Magnetic Iron Carbide Nanoparticles as Effective T2 Contrast Agents. *Nanoscale* **2013**, *6*, 726–730.
- (28) Kresse, G.; Hafner, J. Ab initio Molecular Dynamics for Liquid Metals. *Phys. Rev. B* **1993**, *47*, 558–561.
- (29) Kresse, G.; Hafner, J. Ab initio Molecular-Dynamics Simulation of the Liquid-Metal-Amorphous-Semiconductor Transition in Germanium. *Phys. Rev. B* **1994**, *49*, 14251–14269.

- (30) Kresse, G.; Furthmüller, J. Efficiency of Ab-initio Total Energy Calculations for Metals and Semiconductors Using a Plane-Wave Basis Set. *Comput. Mater. Sci.* **1996**, *6*, 15–50.
- (31) Kresse, G.; Furthmüller, J. Efficient Iterative Schemes for Ab initio Total-Energy Calculations Using a Plane-Wave Basis Set. *Phys. Rev. B* **1996**, *54*, 11169–11186.
- (32) Blöchl, P. E. Projector Augmented-Wave Method. *Phys. Rev. B* **1994**, *50*, 17953–17979.
- (33) Kresse, G.; Joubert, D. From Ultrasoft Pseudopotentials to the Projector Augmented-Wave Method. *Phys. Rev. B* **1999**, *59*, 1758–1775.
- (34) Perdew, J. P.; Burke, K.; Ernzerhof, M. Generalized Gradient Approximation Made Simple. *Phys. Rev. Lett.* **1996**, *77*, 3865–3868.
- (35) Monkhorst, H. J.; Pack, J. D. Special Points for Brillouin-Zone Integrations. *Phys. Rev. B* **1976**, *13*, 5188–5192.
- (36) Methfessel, M.; Paxton, A. T. High-Precision Sampling for Brillouin-Zone Integration in Metals. *Phys. Rev. B* **1989**, *40*, 3616–3621.
- (37) Henkelman, G.; Jónsson, H. A Dimer Method for Finding Saddle Points on High Dimensional Potential Surfaces Using Only First Derivatives. *J. Chem. Phys.* **1999**, *111*, 7010–7022.
- (38) Sheppard, D.; Terrell, R.; Henkelman, G. Optimization Methods for Finding Minimum Energy Paths. *J. Chem. Phys.* **2008**, *128*, 134106.
- (39) Hofer, L. J. E.; Cohn, E. M. Saturation Magnetizations of Iron Carbides. *J. Am. Chem. Soc.* **1959**, *81*, 1576–1582.
- (40) Sorescu, D. C. Plane-Wave Density Functional Theory Investigations of the Adsorption and Activation of CO on Fe₅C₂ Surfaces. *J. Phys. Chem. C* **2009**, *113*, 9256–9274.
- (41) Wulff, G. On the Question of Speed of Growth and Dissolution of Crystal Surfaces. *Z. Kristallogr.* **1901**, *34*, 449–530.
- (42) van Santen, R. A.; Neurock, M. Concepts in Theoretical Heterogeneous Catalytic Reactivity. *Catal. Rev.* **1995**, *37*, 557–698.
- (43) Sung, S. S.; Hoffmann, R. How Carbon Monoxide Bonds to Metal Surfaces. *J. Am. Chem. Soc.* **1985**, *107*, 578–584.
- (44) Hu, P.; King, D. A.; Lee, M. H.; Payne, M. C. Orbital Mixing in CO Chemisorption on Transition Metal Surfaces. *Chem. Phys. Lett.* **1995**, *246*, 73–78.
- (45) van Santen, R. A. Hydrogen Induced CO Activation on Open Ru and Co Surfaces. *Phys. Chem. Chem. Phys.* **2010**, *12*, 6330–6332.
- (46) Torres Galvis, H. M.; Bitter, J. H.; Davidian, T.; Ruitenbeek, M.; Dugulan, A. I.; de Jong, K. P. Iron Particle Size Effects for Direct Production of Lower Olefins from Synthesis Gas. *J. Am. Chem. Soc.* **2012**, *134*, 16207–16215.
- (47) Den Breejen, J. P.; Radstake, P. B.; Bezemer, G. L.; Bitter, J. H.; Frøseth, V.; Holmen, A.; Jong, K. D. On the Origin of the Cobalt Particle Size Effects in Fischer–Tropsch Catalysis. *J. Am. Chem. Soc.* **2009**, *131*, 7197–7203.
- (48) Barkhuizen, D.; Mabaso, I.; Viljoen, E.; Welker, C.; Claeys, M.; van Steen, E.; Fletcher, J. C. Experimental Approaches to the Preparation of Supported Metal Nanoparticles. *Pure Appl. Chem.* **2006**, *78*, 1759–1769.